

A measurement of the intrahalo light fraction with near-infrared background anisotropies

Asantha Cooray¹, Joseph Smidt¹, Francesco De Bernardis¹, Yan Gong¹, Daniel Stern², Matthew L. N. Ashby³, Peter R. Eisenhardt², Christopher C. Frazer¹, Anthony H. Gonzalez⁴, Christopher S. Kochanek⁵, Szymon Kozłowski^{6,5} & Edward L. Wright⁷

¹*Dept. of Physics & Astronomy, University of California, Irvine, CA 92697, USA*

²*Jet Propulsion Laboratory, California Institute of Technology, Pasadena, CA 91109, USA*

³*Harvard-Smithsonian Center for Astrophysics, 60 Garden St., Cambridge, MA 02138, USA*

⁴*Department of Astronomy, University of Florida, Gainesville, FL 32611, USA*

⁵*Department of Astronomy, The Ohio State University, Columbus, OH 43210, USA*

⁶*Warsaw University Observatory, Al. Ujazdowskie 4, 00-478 Warszawa, Poland*

⁷*Department of Physics and Astronomy, University of California, Los Angeles, CA 90095, USA*

Unresolved near-infrared background anisotropies are expected to have contributions from the earliest galaxies during reionization^{1–5} and faint, dwarf galaxies at intermediate redshifts^{6,7}. Previous measurements^{8–12} were unable to conclusively pinpoint the dominant origin because they did not sample spatial scales that were sufficiently large to distinguish between these two possibilities. Here we report a measurement of the anisotropy power spectrum from sub-arcminute to one degree angular scales and find the clustering amplitude to be larger than the model predictions involving the two existing explanations. As the shot-noise level of the power spectrum is consistent with that expected from faint galaxies, a new source population on the sky is not necessary to explain the observations. A physical mechanism that increases the clustering amplitude, however, is needed. Motivated by recent results related to the extended stellar light profile in dark matter halos^{13–15}, we consider the possibility that the fluctuations originate from diffuse intrahalo stars of all galaxies. We find that the measured power spectrum can be explained by an intrahalo light fraction of 0.07 to 0.2% relative to the total luminosity in dark matter halos of 10^9 to 10^{12} solar masses at redshifts of ~ 1 to 4.

In order to distinguish between the two interpretations of the near-IR anisotropy power spectrum, we have analyzed imaging data from the *Spitzer* Deep, Wide-Field Survey (SDWFS)¹⁶. This survey covers 10.5 square degrees on the sky with the IRAC instrument in its four bands between 3.6 and 8 μm . We focus on the data at 3.6 and 4.5 microns as the confusion from zodiacal light limits extragalactic background studies at 5 and 8 microns⁸. The data were taken in four separate epochs between 2004 and 2008 and were conducted in ways to minimize the systematics associated with anisotropy measurements. In particular the four different epochs were observed at different roll angles of the instrument so that the measurements are robust against detector artifacts, persistence resulting from saturated bright stars, and variations in the bias level. The SDWFS mapping strategy was also optimized to facilitate self-calibration¹⁷ of the data by maximizing inter-pixel correlations.

To limit the influence of bright stars and galaxies, including extended sources, in our anisotropy measurements we mask all sources that are detected either in the combined SDWFS data or in the ancillary multi-band optical and near-IR data¹⁸. The effects of mosaicing of individual detector frames, pixelization of the maps, and the detected-source mask are captured by the map-making transfer function (see Supplementary Information). We compute the transfer function and its uncertainty with a large set of sky simulations. The point-spread function (PSF) and its uncertainty were determined by measuring and modeling the PSF of stars at different sub-regions of the image and computing the variance of the differences between the modeled PSFs.

The power spectrum measurements at 3.6 and 4.5 μm show a clear excess above the shot-noise level (Fig. 1). The shot-noise dominates the anisotropy power spectrum at sub-arcminute angular scales corresponding to $\ell > 10^5$. Such a shot-noise is expected from the small-scale Poisson behavior of the spatial distribution of sources on the sky. The clustering amplitude we measure at $\ell \sim 10^4$ is fully consistent with existing measurements of the anisotropy power spectrum with IRAC in deeper, but smaller area, fields^{8,9,12}. At tens of arcseconds angular scales, corresponding to $\ell > 5 \times 10^4$, our shot-noise level is higher than that of a recent measurement by about a factor of 2 because deeper data allow more faint sources to be individually detected and masked¹². Nevertheless, we independently confirm the near-IR background anisotropies at angular scales larger than a few arcminutes at the previously reported amplitude¹².

The near-IR anisotropies have been previously interpreted as either due to spatial clustering of primordial galaxies responsible for cosmic reionization⁸ or due to faint, dwarf galaxies at low redshifts that fall below the individual source detection threshold of *Spitzer* images^{6,7,9}. Fig. 1 shows that the measured fluctuations in SDWFS are well above both these interpretations. The power spectrum predictions for $z > 6$ galaxies rely on a combination of analytical calculations¹⁹ and numerical simulations²⁰ of reionization. If we force the $z > 6$ galaxy model to fit the power spectrum data then the integrated intensity of $z > 6$ galaxies is about $2 \text{ nW m}^{-2} \text{ sr}^{-1}$ at 3.6 μm ¹⁹. In order to reach such a high intensity these galaxies must be very efficient in converting baryons to stars²⁰. In fact, the required star-formation rate conflicts with the measured metal abundance at $z > 4$, the measured X-ray background when compared to X-rays from stellar end products such as black holes, and the measured luminosity functions of bright Lyman-dropout galaxies²¹. Unless a significant revision of our current understanding of $z > 6$ galaxy statistics is made it is unlikely that the measured anisotropy power spectrum is dominated by the primordial galaxies.

The prediction for low redshift, faint galaxy intensity fluctuations involves a large compilation of multi-wavelength luminosity functions and galaxy number counts⁷. The measured luminosity function slope at the faint-end is used to extrapolate to the fainter galaxies that are undetected in the *Spitzer* images. An increase in the faint-end slope above the measured values does not increase the clustering amplitude on the angular scales of interest without modifying the shot-noise level. While the clustering amplitude is smaller than the measurements, the prediction related to faint, dwarf galaxies⁷ shows that they generate a shot-noise level consistent with the measured small-scale anisotropy power spectrum (Fig. 1). At few tens arcminute angular scales the measurements

are such that the clustering amplitude is about a factor of 6 to 10 above the prediction. While this difference suggests that a new model to explain the anisotropy power spectrum is clearly needed, the consistency with the shot-noise level is such that we do not need to invoke a new population of point sources on the sky to explain the observations.

While keeping the shot-noise level the same, the measurements can be explained by any physical effect that boosts the two-halo term of clustering. One possibility is to increase the halo mass scale of the faint, dwarf galaxies so that clustering bias factor is increased. The required modification needed to explain the fluctuations data, however, is ruled out by the measured number counts and the redshift distribution⁷. Since intensity anisotropies are measured, another option is to introduce a luminosity component to the dark matter halos that remain unmasked when the hosted bright galactic disks are masked as part of the analysis. Such a possibility exists in the literature in the form of diffuse halo stars in the extended stellar profile of galaxies out to distances of 100 kpc²². In our anisotropy measurements, we mask the faintest detected galaxies to 3-4'' which removes the light from the bulges and disks of those galaxies. To remove the diffuse light component we would have to mask to a radius greater than 10'' around each galaxy. The surface density of galaxies down to $m_{AB} < 22$ at 3.6 μm is such that we expect 2 to 3 galaxies within a circle of radius 10''. Thus masks which successfully remove the diffuse component leave no pixels on the map from which to measure the anisotropy power spectrum.

Existing studies discuss this extended emission in terms of the diffuse intrahalo light (IHL)¹⁵ and explain the origin through tidally stripped stars during galaxy mergers and collisions. The stripped fraction is expected to be a function of the halo mass with more massive halos containing a larger fraction of the diffuse halo emission^{13,14,23}. On galaxy cluster scales the diffuse intracluster light^{24,25} is a significant fraction of the total luminosity of the cluster. We describe the intensity anisotropy power spectrum from the IHL by modifying the standard galaxy clustering predictions²⁸ to include a profile for the diffuse stars in halos (see Section 8 of the Supplementary Information). If the clustering excess in near-IR anisotropy power spectrum is due to IHL, then we find that measured anisotropies can be described with halos in the mass range of 10^9 to $10^{12} M_\odot$. Averaged over this mass range we find an f_{IHL} of 0.07 to 0.2% at 68% confidence level (Fig. 2). The implied fraction is consistent with the theoretical expectation that the IHL level is small for low mass halos, but differences also exist with current theory predictions^{13,14}, especially in terms of the power-law slope of the halo mass dependence.

If this new interpretation involving IHL is the correct description of measured IR background anisotropies, we find that the IHL in all dark matter halos that we are probing contribute $0.75 \pm 0.25 \text{ nW m}^{-2} \text{ sr}^{-1}$ to the total intensity at 3.6 μm . This intensity can be compared to the rms fluctuations of about $0.1 \text{ nW m}^{-2} \text{ sr}^{-1}$ at a few arcminutes angular scale (see Fig. 3). The IHL fluctuation signal varies spatially at a level of 10 to 15% of its integrated intensity and below 1% of the total background intensity of $13.3 \pm 2.8 \text{ nW m}^{-2} \text{ sr}^{-1}$ at 3.6 μm ²⁹. As the spectral energy distribution of IHL is mostly unknown, we make use of a variety of SEDs from B to K-type stellar spectral templates and find an order of magnitude variation at wavelengths of $\sim 1 \mu\text{m}$ (Fig. 3). In all

these cases we predict the existence of optical background light fluctuations. They will have a similar power spectrum shape and will be fully correlated with fluctuations at $3.6\ \mu\text{m}$. Furthermore the near-IR anisotropies we have measured should be correlated with the sub-mm anisotropies³⁰, especially if there are diffuse and extended dust associated with galaxies. These form future tests that can be used to improve our understanding of the content and nature of IHL in distant dark matter halos.

1. Santos, M. R., Bromm, V. & Kamionkowski, M. The contribution of the first stars to the cosmic infrared background, *Mon. Not. R. Astron. Soc.* 336, 1082-1092 (2002).
2. Salvaterra, R. & Ferrara, A. The imprint of the cosmic dark ages on the near-infrared background, *Mon. Not. R. Astron. Soc.* 339, 973-982 (2003).
3. Cooray, A., Bock, J. J., Keating, B., Lange, A. E. & Matsumoto, T. First Star Signature in Infrared Background Anisotropies, *Astrophys. J.* 606, 611-624 (2004).
4. Kashlinsky, A., Arendt, R., Gardner, J. P., Mather, J. C. & Moseley, S. H. Detecting Population III Stars through Observations of Near-Infrared Cosmic Infrared Background Anisotropies, *Astrophys. J.* 608, 1-9 (2004).
5. Fernandez, E. R., Komatsu, E., Iliev, I. T., Shapiro, P. R. The Cosmic Near-Infrared Background II: Fluctuations, *Astrophys. J.* 710, 1089-1110 (2010).
6. Chary, R., Cooray, A. & Sullivan, I. Contribution to Unresolved Infrared Fluctuations from Dwarf Galaxies at Redshifts of 2-3, *Astrophys. J.* 681, 53-57 (2008).
7. Helgason, K., Ricotti, M. & Kashlinsky, A. Reconstructing the Near-IR Background Fluctuations from known Galaxy Populations using Multiband Measurements of Luminosity Functions, *arXiv:1201.4398*
8. Kashlinsky, A., Arendt, R. G., Mather, J. & Moseley, S. H. Tracing the first stars with fluctuations of the cosmic infrared background, *Nature*, 438, 45-50 (2005).
9. Cooray, A., Sullivan, I., Chary, R., Bock, J. J., Dickinson, M., Ferguson, H. C., Keating, B., Lange, A., et al. IR Background Anisotropies in Spitzer GOODS Images and Constraints on First Galaxies, *ApJL*, 659, L91-L94 (2007).
10. Thompson, R., Eisenstein, D., Fan, X., Rieke, M. & Kennicutt, R. C. Evidence for a $z < 8$ Origin of the Source-subtracted Near-Infrared Background, *Astrophys. J.* 666, 658 (2007).
11. Matsumoto, T. et al. AKARI Observation of the Fluctuation of the Near-infrared Background, *Astrophys. J.* 742, 124 (2011).
12. Kashlinsky, A. et al. New measurements of the cosmic infrared background fluctuations in deep Spitzer/IRAC survey data and their cosmological implications, *arXiv:1201.5617*

13. Purcell, C. W., Bullock, J. S. & Zentner, A. R. Shredded Galaxies as the Source of Diffuse Intrahalo Light on Varying Scales, *Astrophys. J.* 666, 20-33 (2007)
14. Purcell, C. W., Bullock, J. S. & Zentner, A. R. The Metallicity of Diffuse Intrahalo Light, *Mon. Not. R. Astron. Soc.* 391, 550-560 (2008).
15. Conroy, C., Wechsler, R. H. & Kravtsov, A. V. The Hierarchical Build-Up of Massive Galaxies and the Intracluster Light since $z=1$, *Astrophys. J.* 668, 826-838 (2007).
16. Ashby, M. L. N. et al. The Spitzer Deep, Wide-field Survey. *Astrophys. J.* 701, 428-453 (2009).
17. Arendt, R. G., Fixsen, D. J. & Moseley, S. H. Dithering Strategies for Efficient Self-Calibration of Imaging Arrays, *Astrophys. J.* 536 500-512 (2000).
18. Jannuzi, B. T. & Dey, A. Photometric Redshifts and the Detection of High Redshift Galaxies, ASP Conference Series, Vol. 191, Edited by R. Weymann, L. Storrie-Lombardi, M. Sawicki, & R. Brunner. ISBN: 158381-017-X, p. 111 (1999)
19. Cooray, A., Gong, Y., Smidt, J. & Santos, M. G. The Near-IR Background Intensity and Anisotropies During The Epoch of Reionization, *Astrophys. J.* in press, arXiv:1205.2316 (2012).
20. Fernandez, E. R., Iliev, I. T., Komatsu, E. & Shapiro, P. R. The Cosmic near Infrared Background. III. Fluctuations, Reionization, and the Effects of Minimum Mass and Self-regulation, *Astrophys. J.* 750, 20 (2012).
21. Madau, P. & Silk, J. Population III and the near-infrared background excess, *Mon. Not. R. Astron. Soc.* 359, L37-L41 (2005).
22. Tal, T. & Dokkum, P. The faint stellar halos of massive red galaxies from stacks of more than 42000 SDSS LRG images, *Astrophys. J.* 731, 89 (2011).
23. Lin, Y. & Mohr, J. J. K-band Properties of Galaxy Clusters and Groups: Brightest Cluster Galaxies and Intracluster Light, *Astrophys. J.* 617, 879-895 (2004).
24. Rudick, C. S., Mihos, J. C., Frey, L. H. & McBride, C. K. Tidal Streams of Intracluster Light, *Astrophys. J.* 699, 1518-1529 (2009).
25. Gonzalez A. H. , Zabludoff A. I. & Zaritsky D. , Intracluster light in nearby galaxy clusters: Relationship to the halos of brightest cluster galaxies, *Astrophys. J.* 618, 195-204 (2004).
26. Carollo, D., et al. Structure and Kinematics of the Stellar Halos and Thick Disks of the Milky Way Based on Calibration Stars from Sloan Digital Sky Survey DR7, *Astrophys. J.* 712, 692-727 (2010).
27. Courteau, S. et al. The Luminosity Profile and Structural Parameters of the Andromeda Galaxy, *Astrophys. J.* 739, 20 (2011).

28. Cooray, A. & Sheth, R. Halo models of large scale structure. *Physics Reports*, 372, 1-129 (2002).
29. Levenson, L. R., Wright, E. L. & Johnson, B. D. DIRBE Minus 2MASS: Confirming the CIRB in 40 New Regions at 2.2 and 3.5 Microns, *Astrophys. J.* 666, 34-44 (2007).
30. Amblard, A. et al. Submillimetre galaxies reside in dark matter haloes with masses greater than 3×10^{11} solar masses, *Nature*, 470, 510-512 (2011).

Acknowledgements We acknowledge support from NSF CAREER (to A.C.), NASA ADAP, and an award issued by JPL/Caltech. We thank R. Arendt for sharing his IRAC self-calibration code. We thank J. Bock and M. Zemcov for their contributions to the SDWFS project. This work is based on observations made with the Spitzer Space Telescope. This work also made use of data products provided by the NOAO Deep Wide-Field Survey. A.C. thanks the Aspen Center for Physics for hospitality.

Author Contributions A.C. planned the study, developed the intrahalo light model, supervised the research work of J.S., F.D. C.F. and Y.G., and wrote the draft version of this paper. J.S. and C.F. performed the power spectrum measurements and F.D. interpreted those measurements with a halo model for the intrahalo light. Y.G. developed a model for the high-redshift galaxies. All other coauthors of this paper contributed extensively and equally by their varied contributions to the SDWFS project (led by D.S. as the PI), planning of SDWFS observations, analysis of SDWFS data, and by commenting on this manuscript as part of an internal review process.

Correspondence Correspondence and requests for materials should be addressed to A.C. (acooray@uci.edu)

Competing interests statement The authors declare no competing interests.

Supplementary information accompanies this paper.

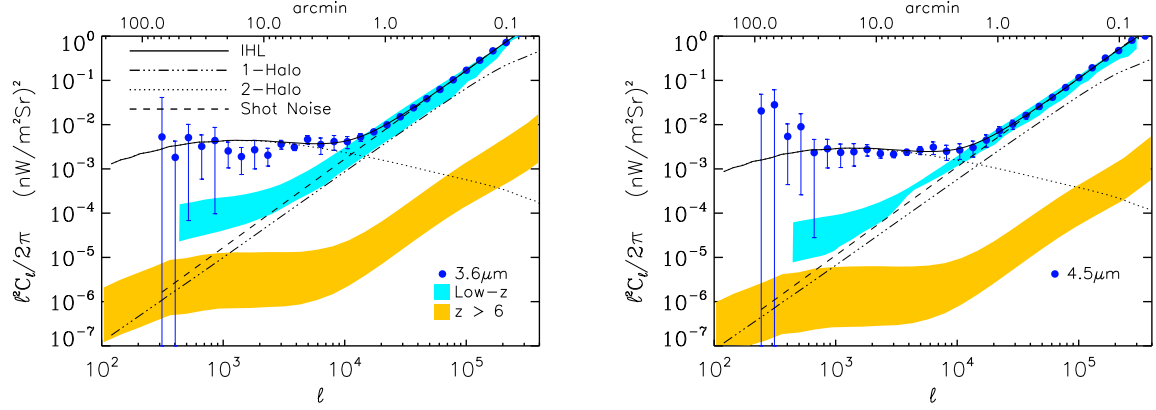


Figure 1: The angular power spectrum of the unresolved near-IR background. The total power spectrum $P(k)$ of SDWFS at $3.6 \mu\text{m}$ (top) and $4.5 \mu\text{m}$ (bottom) as a function of the multipole moment. SDWFS imaging data were taken on the same field at four separate epochs in January 2004, August 2007, February 2008, and March 2008. Each epoch of data, taken over 7 to 10 days, includes 4300 to 4900 IRAC frames that were combined to make mosaics using the self-calibration algorithm¹⁷. The total integration time is 6 minutes per pixel. These individual frames were first visually inspected and cleaned of artifacts such as asteroidal trails and hot pixels. Through cross-correlations between sum and difference maps between epochs, we make independent measurements of the sky signal and noise. The final power spectrum is the average of the multi-epoch cross-correlation data under the assumption that the instrumental noise is not correlated between epochs. In both panels the error bars are 1σ uncertainties in the power spectrum. They are determined by propagating the errors from the beam measurement into the power spectrum, while the simulations, based out of noise measurements, were used to obtain instrumental and sky variance. The quadratic sum of these errors and the map-making transfer function uncertainty constitutes the final error estimate. The two shaded regions show the expected contribution from $z > 6$ galaxies¹⁹ and low-redshift galaxies⁷ based on two model predictions in the literature. The lines show a diffuse intrahalo light model where we show the signal in terms of the total (solid), one (dashed-dotted) and two (dotted) halo terms. The dashed line is the best-fit shot-noise signal that dominates the anisotropies at small angular scales.

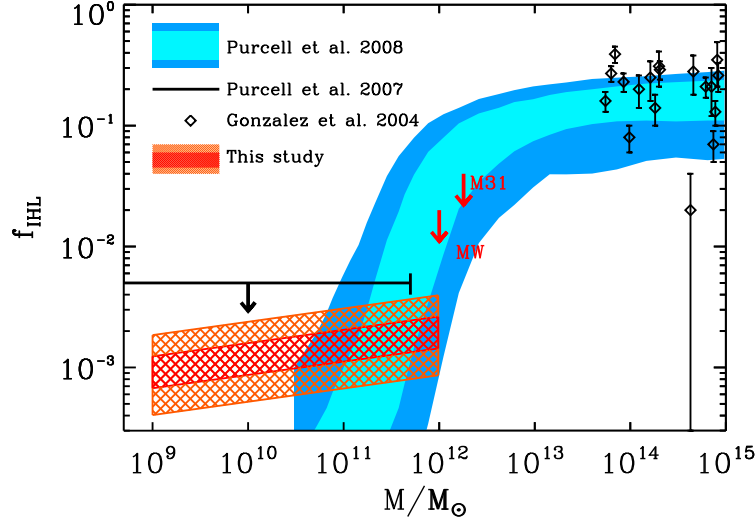


Figure 2: **The intrahalo light fraction from diffuse stars as a function of the halo mass.** The dark and light blue shaded regions show the 95% and 68% range of f_{IHL} relative to the total luminosity of the dark matter halos as a function of the halo mass from an analytical prediction¹⁴, valid for $f_{\text{IHL}} > 4 \times 10^{-4}$ and $M > 5 \times 10^{10} M_{\odot}$ and at $z = 0$. We show the case where subhalos on orbits passing within a critical radius of the host halo center contribute their light to the central galaxy rather than to the diffuse component. We also show a prediction where f_{IHL} is constant¹³, due to dwarf galaxies that are completely destroyed, with a value ~ 0.005 when $M \lesssim 5 \times 10^{11} M_{\odot}$ (solid line fixed at $f_{\text{IHL}} = 5 \times 10^{-3}$). The downward arrow indicates the possibility that the constant f_{IHL} value for low mass halos may be smaller at higher redshifts. The red and orange hatched regions at the bottom of the plot are the preferred 68% and 95% confidence level range, respectively, on f_{IHL} from our analysis of the SDWFS near-IR anisotropy power spectrum. The mass range is determined by the minimum and maximum halos masses consistent with the halo model fit that includes the IHL component. Both the mass and f_{IHL} ranges are valid over the broad redshift interval from $z = 1$ to 4 over which the anisotropy signal is generated. We do not find a significant halo mass dependence on the IHL fraction with the mass-dependent power-law to be 0.09 ± 0.01 between 10^9 to $10^{12} M_{\odot}$, consistent with the possibility that f_{IHL} is mass independent¹³ when $M \lesssim 5 \times 10^{11} M_{\odot}$. Our model requires the total luminosity-halo mass relation to evolve with redshift as $(1 + z)^{1.2 \pm 0.1}$. This luminosity evolution with redshift can also be absorbed into the evolution of $f_{\text{IHL}}(M)$ evolution with redshift. For reference, we also show measurements and 1σ errors of the intracluster light²⁵, the galaxy group and cluster analog for IHL when $M > 5 \times 10^{13} M_{\odot}$. At halo masses around $10^{12} M_{\odot}$ we show the 95% confidence level upper limit on f_{IHL} estimated for Milky Way²⁶ and Andromeda (M31)²⁷.

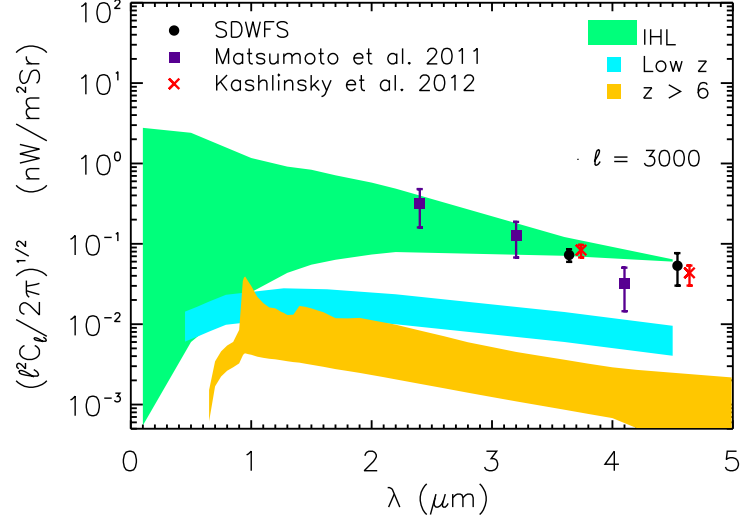


Figure 3: **The spectral energy distribution of IR background anisotropies.** The frequency spectrum of near-IR and optical background anisotropies as a function of the wavelength. We show the rms fluctuation amplitude at $\ell = 3000$, corresponding to fluctuations at 6 arcminute angular scales. We show our measurement and the existing measurements in the literature at the same angular scales^{11,12}. The plotted error bars are the 1σ uncertainties directly propagated to a rms fluctuation amplitude from the power spectrum errors. We do not show the measurements at 1.6 and $1.1 \mu\text{m}$ ¹⁰ as they do not probe fluctuations on scales greater than 2 arcminutes on the sky due to the narrow field of view of the observations. The shaded regions are (a) predictions for the IHL taking a variety of spectral energy distributions for the stripped stars (green), (b) $z > 6$ galaxies (yellow), and (c) low-redshift galaxies below the detection level of masking (blue).

Supplementary Information

In these Supplemental Notes to the main paper, we outline key details related to how we estimated the angular power spectrum of *Spitzer*/IRAC data and its interpretation. The data used for this study are publicly available from the Spitzer Heritage Archive¹ under the program number GO 40839 (PI. D. Stern).

1 The Spitzer Deep Wide Field Survey

We use the IRAC data from the Spitzer Deep Wide Field Survey (SDWFS)^{16,31}. Of the NDWFS Boötes fields, the observations were obtained in 4 epochs, with depth per pixel of 90 seconds in each epoch. Each epoch took observations over 7 to 10 days to complete the full mosaic. We started with the basic calibrated data (BCDs). At each epoch, imaging data was obtained in all four IRAC wavelengths or channels (3.6, 4.5, 5.8, and 8 μm); however, for this study we focus on the 3.6 and 4.5 μm data. Each epoch consists of 4300 to 4900 BCDs per channel that were mosaiced to form the final images used in the fluctuation analysis.

Instead of using the public SDWFS mosaics (Available at <http://irsa.ipac.caltech.edu>), made with the standard *Spitzer* data analysis pipeline MOPEX³², we produced our own mosaics in order to better control systematic errors. To mosaic the BCDs for each channel and epoch we used a self-calibration algorithm^{17,33} to properly match the sky background level from one adjacent frame to the other in the overlapping region using an optimized least squares fitting technique. The SDWFS mapping strategy incorporates several elements to facilitate self-calibration of the data by maximizing inter-pixel correlations. We dithered the observations on small scales and offset by one-third of an IRAC field-of-view between successive passes through each group. This provides inter-pixel correlation information on both small and large scales, so the self-calibrated mosaic has background levels that are stable across the wide area of the SDWFS mosaic. Finally, for the larger, rectangular groups, we cadence the observations such that revisits cover the same area but with a different step size. With a $< 10\%$ penalty in mapping efficiency, cadencing significantly enhanced the inter-pixel correlations across all scales.

These mapping strategies were designed to significantly enhance the self-calibration of the data. Finally, by reobserving the field multiple times at different roll angles, our observing strategy was designed to be robust against bad rows/columns, large scale cosmetic defects on the array, after-images resulting from saturation due to bright stars, variations in the bias level, and the color dependence of the IRAC flat-field across the array³⁴. In particular, the challenging diffuse background measurements we report here are vastly aided by the redundant coverage: independent data sets of the same region are the best way to assess and control systematic errors. With this mapping strategy we were able to construct independent sky realizations for carrying out jackknife testing.

¹<http://sha.ipac.caltech.edu/applications/Spitzer/SHA/>

Furthermore, the power spectrum is estimated by cross-correlating the maps from different epochs, eliminating bias from uncorrelated signals such as instrumental noise and mosaicing artifacts.

For each IRAC channel and epoch we passed the cleaned BCD into our self-calibration code, a slightly modified version of an existing code¹⁷, as inputs the cleaned BCDs (cBCDs) with the final, output array size and astrometry defined to correspond to the mosaic of first 3.6 μm epoch. The cBCDs were first cleaned of asteroid trails, hot pixels, and other image artifacts. Since the astrometry is the same for each mosaic, they can be properly coadded and jack-knifed as described below. Each of the cBCDs have an angular pixel scale of 1.2 arcseconds, which was preserved in the final mosaics. The portion of the maps used for analysis are $\sim 3.5 \times 3$ degrees on a side for a total area of ~ 10.5 square degrees. The final mosaics generated from the self-calibration algorithm are shown in Fig. S1.

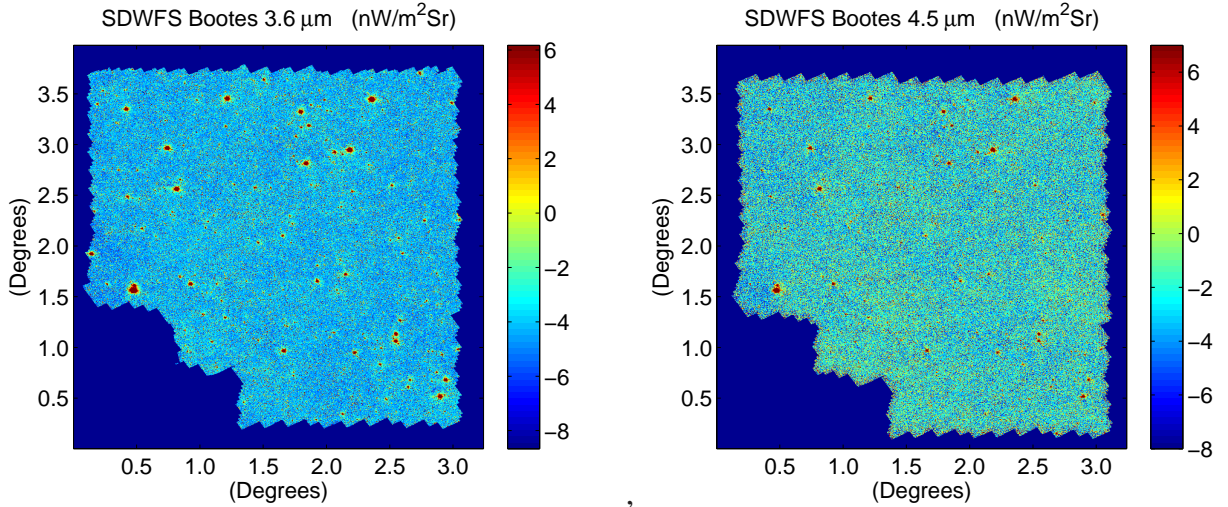


Figure S 1: **The SDWFS Maps.** The final 3.6 μm (left) and 4.5 μm (right) self-calibrated mosaics used for the Boötes SDWFS analysis.

2 Generation of the Detected Source Mask

As the analysis concentrates on the background intensity fluctuations, with the aim of identifying the nature of faint sources below the individual detection level, we must remove the contamination from individual detected sources in our power spectrum measurement. We created source masks based both on the objects detected in the IRAC data at 3.6 and 4.5 μm and the NOAO Deep Wide Field Survey (NDWFS) catalogs for the B_w , R and I bands. The masked sources include stellar point sources, galaxies that are extended, and galaxies that are unresolved but detected as point sources in SDWFS. The mask also accounts for the Spitzer-IRAC point spread function (PSF). For this study we make use of the publicly available "extended" IRAC PSF to properly account for flux wings.

Next, we summarize our recipe to generate the source list and discuss more details below:

1. We create a catalog consisting of all objects detected by SExtractor at a 3σ detection threshold on the coadded and individual epoch maps at both 3.6 and $4.5 \mu\text{m}$.
2. We add any additional objects detected in the NDWFS optical catalogs, but missing from the IRAC catalogs.
3. We create a map initially of zeros where we place each source detected from our combined catalogs with the proper flux values. The sources that are flagged as extended in the SExtractor catalogs are placed as extended sources with a size that is comparable to their estimated size.
4. We convolve this final map with the IRAC PSF to ensure that the flux wings for each source are properly masked.
5. We make a cut at a certain flux level so that all pixels with intensity down to that threshold are masked. We then histogram the remaining pixels from the data map and cut all pixels that are $\pm 5 \sigma$ away in the histogram. The latter step is similar to prior approaches to measure the *Spitzer*-IRAC background anisotropy power spectrum³⁶.
6. To produce the final mask, we set the pixels with intensity values above the final flux and outliers from histogram to a value of zero, and the remaining pixels, the ones used for anisotropy measurements, a value of one.

Before the mosaics were created, source extractor was run iteratively on each epoch and waveband individually as well as on the coadded maps for both wavebands in order to find detected sources. The parameters used for SExtractor are the same as the ones used for the original SDWFS catalogs¹⁶. The combined catalog obtained from this iterative source extractor analysis, as well as the objects detected in the NDWFS catalog are merged into a final catalog.

The final flux cut for the mask was found iteratively by lowering the flux limit until further expansions of the masked regions no longer affect the final power spectrum. Since the PSF is slightly different for the $3.6\mu\text{m}$ and $4.5\mu\text{m}$ wavebands the two masks are independently constructed. Fig. S2 shows the final masked epoch 1 maps. The final mask is such that 56% of the original pixels are removed from the subsequent analysis.

3 Power Spectrum Estimation

With the final mosaics and masks in hand, initial, raw auto and cross-correlations may be computed to measure the level of clustering in the maps at each scale. To calculate the cross-correlation

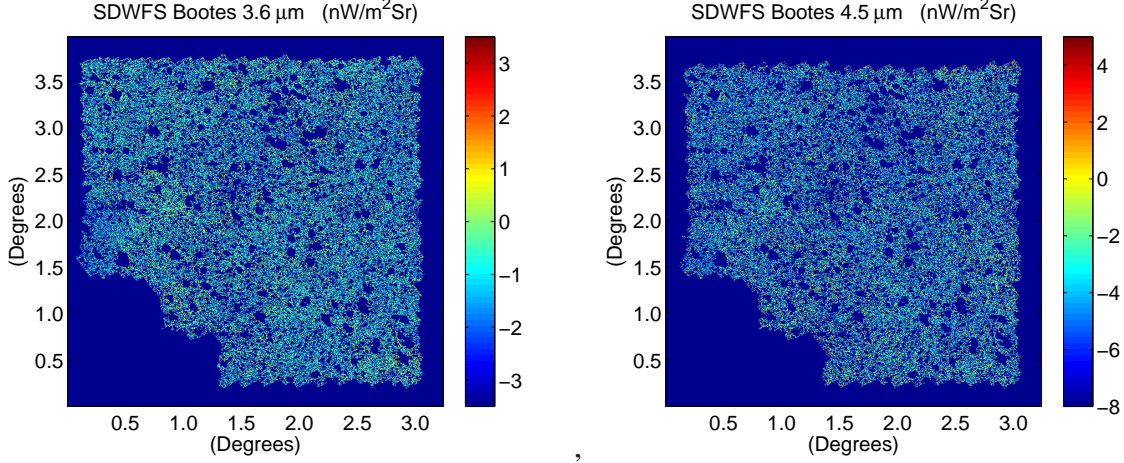


Figure S 2: **The Masked SDWFS maps.** The final 3.6 μm (left) and 4.5 μm (right) masked maps used for the Boötes SDWFS analysis. The mask used for the analysis removes 56% of the pixels in the mosaic.

between masked maps M_1 and M_2 in real space, we first take the 2D Fourier transform of each map which we call \tilde{M}_1 and \tilde{M}_2 , as

$$\tilde{M}[l_x, l_y] = \Delta \sum_{m=0}^{M-1} \sum_{n=0}^{N-1} M[m, n] e^{-2\pi i(l_x m/M + l_y n/N)} \quad (1)$$

where M and N are the number of discrete points in the two dimensions of the map and Δ is the sampling interval in radians. The power spectra C_l formed from the cross-correlation of M_1 and M_2 for a specific l_i bin between between l -modes l_1 and l_2 is equal to the weighted mean of the squared Fourier modes $\tilde{M}_1 \tilde{M}_2^*$ between l_1 and l_2 ,

$$C_{l_i} = \frac{\sum_{l_x^2 + l_y^2 \leq l_2} \sum_{l_x^2 + l_y^2 \geq l_1} w[l_x, l_y] \tilde{M}_1[l_x, l_y] \tilde{M}_2^*[l_x, l_y]}{\sum_{l_x^2 + l_y^2 \leq l_2} \sum_{l_x^2 + l_y^2 \geq l_1} w[l_x, l_y]}, \quad (2)$$

where $w[l_x, l_y]$ is a window function in Fourier space that is non-zero for each mode of the analysis and zero for modes that are discarded. To compute the raw auto-correlation we have the special case where $M_1 = M_2$.

Being able to form a power spectrum from a cross-correlation rather than an auto-correlation is highly advantageous, as the noise bias and other contaminants that can dominate an auto-correlation calculation are minimized in a cross-correlation. This is because the pixel of each map $M_i = S_i + N_i$ is really a sum of the signal S_i plus noise N_i . The noise contributes to the auto-correlation such that $M_1 \times M_1 = S_1^2 + N_1^2$, but is minimized in a cross-correlation $M_1 \times M_2 = (S_1 + N_1) \times (S_2 + N_2) = S_1^2$, since $S_1 = S_2$. Another advantage to a cross-correlation study in this analysis is the availability of multi-epoch data over a four-year period. In

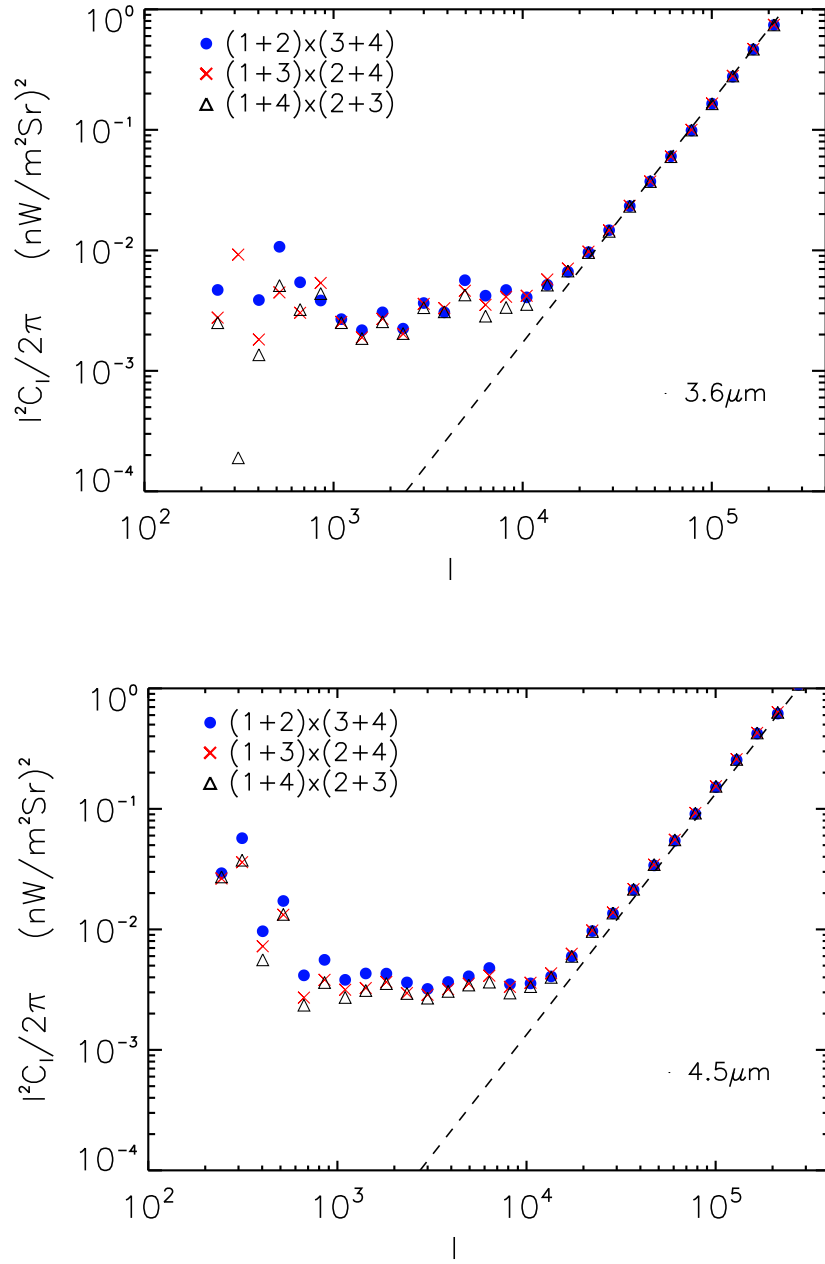


Figure S 3: **The cross power spectra of the sum of multi-epoch maps.** The cross-correlation power spectra of different epoch summed maps with $3.6 \mu\text{m}$ (top) and $4.5 \mu\text{m}$ (bottom) shown separately. The average of the summed maps are taken to be the power spectrum. The notation $(a+b) \times (c+d)$ indicates a cross correlation between the average of the $a+b$ and the $c+d$ epochs.

such data any time varying signals that are not correlated between epochs cannot contribute to the background anisotropy power spectrum. One such possibility is the zodiacal light associated with scattered Sunlight off of dust particles. This is due to dynamical dust particles in near-Earth orbits. Furthermore with varying *Spitzer* orbit the lines of sights to the SDWFS Boötes field during the four epochs will also be different. Thus, we expect the zodiacal light contamination to have a time varying component that is not correlated between epochs. While autocorrelations in single epochs may be contaminated by zodiacal light, we expect cross-correlations to reduce the contamination. A previous analysis³⁶ showed that the contamination from zodiacal light spatial fluctuations is at least an order of magnitude below the background anisotropy level at $3.6 \mu\text{m}$. Thus, zodiacal light should not be the dominant systematic effect in the present analysis. The cross-correlations using sum maps of epochs 1 to 4 are shown in Fig. S3.

We can check the assumption that $N_1 \times N_2$ terms cancel by examining the cross-correlation between, say, $M_1 - M_2 = N_1 - N_2$ and $M_3 - M_4 = N_3 - N_4$. For differences of the same region the signal terms cancel and the amplitude of the cross-correlation $(M_1 - M_2) \times (M_3 - M_4)$ provides an estimate for the floor level at which noise contributions cancel. In Fig. S4 we show these differences, where we find that the cross-correlation power spectra between different epoch differences are consistent with zero. The variance of these difference cross-correlations provide a part of the error budget associated with noise correlations between different epochs including any systematic effects that are not canceled out in difference maps and are correlated between epochs. Since these spectra represent the noise floor the absolute value, we add them to the final error budget in quadrature with other uncertainties (Fig. S5).

Even after cross-correlation, the raw spectra are contaminated by several different sources and require additional corrections. These issues include resolution damping from the beam, the fictitious correlations introduced by the mask and shot noise. All three of these contaminants are dealt with as described below.

4 The Beam Correction

The first correction that needs to be applied to the raw power spectra is the correction for the beam. Realistic detectors have limits to their resolving power which causes a fictitious drop in power at high multipoles. For a known beam structure, the resolution limits of the instrument can be modeled in harmonic space with a function that encodes the full-width-half-max (FWHM) of the telescope. The resulting scale dependent function is known as the beam transfer function, b_l . For a Gaussian beam it can be computed analytically as

$$b_l = \exp(l^2 \sigma_{\text{beam}}^2 / 2) \quad \text{and} \quad (3)$$

$$\sigma_{\text{beam}} = \frac{\theta_{\text{FWHM}}}{\sqrt{8 \ln 2}}, \quad (4)$$

where θ_{FWHM} encodes the full-width-half-max of the instrument's resolving power. The Spitzer team has measured $\theta_{\text{FWHM}} = 1.9$ arcsec. The beam transfer function can also be computed directly from the data by measuring the point spread function. Each bright point source in the sky really shines a thin point like beam of light that should only illuminate a single pixel of the detector. However, due to the finite resolution of the telescope, the source is spread out over many pixels and often has a complex shape very different from a Gaussian. Fig. S6 shows this is true of the SDWFS PSF, and for this reason the beam transfer function needs to be calculated directly from the PSF.

In general, the beam transfer function b_l in Fourier or multipolar space is

$$b_l^2 = \frac{C_l^{M_{\text{psf}}}}{C_l^{M_{\text{point}}}} \quad (5)$$

where $C_l^{M_{\text{psf}}}$ is the power spectrum of M_{psf} , the observed image of a point source including the effects of the telescope, and $C_l^{M_{\text{point}}}$ is the power spectrum of a true point source where all the light lies in one pixel of the map. Fig. S7 shows the beam calculated using Eq. 5 and the publicly available models of the *Spitzer*-IRAC PSF. The PSFs differ for each epoch and waveband and the appropriate beam transfer function for a cross-correlation between maps M_1 and M_2 becomes:

$$b_l^{1 \times 2} = \sqrt{b_l^1 b_l^2} \quad (6)$$

where b_l^1 and b_l^2 are the beam transfer functions for maps M_1 and M_2 respectively.

The beam corrected spectra C_l are then computed from the raw power spectrum C_l^{raw} by dividing by the beam transfer function b_l ,

$$C_l = C_l^{\text{raw}} / b_l^2. \quad (7)$$

To measure the uncertainty in the beam transfer function we must understand the uncertainties in the PSF. The SDWFS team provides several measured PSFs taken across the Boötes images from which the uncertainty in b_l can be measured from Eq. 5 as $\delta b_l = \delta C_l^{M_{\text{psf}}} / C_l^{M_{\text{point}}}$ with $\delta C_l^{M_{\text{psf}}}$ estimated from the variance of the differences from using the various PSF models.

5 The Mode Coupling Correction.

Fictitious correlations introduced by the mask must be corrected. When an image is masked, the sources are replaced by the value zero in the image. When the power spectrum is computed, these zeros in real space make fictitious contributions to the two-dimensional Fourier transform that are then added to the final power spectrum. This can be easily seen in Fig. S9. On the top we see an unmasked fluctuation pattern for a specific l -mode. After the mask is applied, this fluctuation gets broken up into fluctuations of different sizes causing both a diminishing and a reshuffling of power in Fourier space.

l_{eff}	$l^2 C_l / 2\pi$ (3.6 μm) [$\text{nW m}^{-2} \text{sr}^{-1}$] ²	$l^2 C_l / 2\pi$ (4.5 μm) [$\text{nW m}^{-2} \text{sr}^{-1}$] ²
243	$(0.27 \pm 0.36) \times 10^{-2}$	$(2.04 \pm 2.82) \times 10^{-2}$
313	$(0.52 \pm 0.58) \times 10^{-2}$	$(2.81 \pm 3.33) \times 10^{-2}$
402	$(0.18 \pm 0.24) \times 10^{-2}$	$(0.54 \pm 0.49) \times 10^{-2}$
517	$(0.51 \pm 0.50) \times 10^{-2}$	$(0.89 \pm 0.87) \times 10^{-2}$
665	$(0.32 \pm 0.26) \times 10^{-2}$	$(0.23 \pm 0.23) \times 10^{-2}$
854	$(0.43 \pm 0.42) \times 10^{-2}$	$(0.28 \pm 0.18) \times 10^{-2}$
1099	$(0.25 \pm 0.12) \times 10^{-2}$	$(0.23 \pm 0.12) \times 10^{-2}$
1412	$(0.18 \pm 0.11) \times 10^{-2}$	$(0.24 \pm 0.12) \times 10^{-2}$
1815	$(0.26 \pm 0.16) \times 10^{-2}$	$(0.27 \pm 0.08) \times 10^{-2}$
2332	$(0.19 \pm 0.09) \times 10^{-2}$	$(0.21 \pm 0.04) \times 10^{-2}$
2997	$(0.34 \pm 0.08) \times 10^{-2}$	$(0.20 \pm 0.03) \times 10^{-2}$
3851	$(0.29 \pm 0.05) \times 10^{-2}$	$(0.22 \pm 0.04) \times 10^{-2}$
4949	$(0.43 \pm 0.09) \times 10^{-2}$	$(0.24 \pm 0.05) \times 10^{-2}$
6360	$(0.32 \pm 0.13) \times 10^{-2}$	$(0.28 \pm 0.09) \times 10^{-2}$
8173	$(0.36 \pm 0.13) \times 10^{-2}$	$(0.22 \pm 0.08) \times 10^{-2}$
1.05×10^4	$(0.34 \pm 0.10) \times 10^{-2}$	$(0.22 \pm 0.09) \times 10^{-2}$
1.35×10^4	$(0.42 \pm 0.08) \times 10^{-2}$	$(0.25 \pm 0.10) \times 10^{-2}$
1.735×10^4	$(0.53 \pm 0.05) \times 10^{-2}$	$(0.35 \pm 0.11) \times 10^{-2}$
2.229×10^4	$(0.72 \pm 0.03) \times 10^{-2}$	$(0.54 \pm 0.12) \times 10^{-2}$
2.865×10^4	$(1.02 \pm 0.04) \times 10^{-2}$	$(0.71 \pm 0.16) \times 10^{-2}$
3.682×10^4	$(1.49 \pm 0.04) \times 10^{-2}$	$(1.03 \pm 0.17) \times 10^{-2}$
4.731×10^4	$(2.14 \pm 0.03) \times 10^{-2}$	$(1.48 \pm 0.19) \times 10^{-2}$
6.081×10^4	$(3.05 \pm 0.03) \times 10^{-2}$	$(2.10 \pm 0.15) \times 10^{-2}$
7.814×10^4	$(4.28 \pm 0.05) \times 10^{-2}$	$(2.97 \pm 0.13) \times 10^{-2}$
1.004×10^5	$(5.87 \pm 0.06) \times 10^{-2}$	$(4.11 \pm 0.14) \times 10^{-2}$
1.291×10^5	$(7.67 \pm 0.09) \times 10^{-2}$	$(5.27 \pm 0.12) \times 10^{-2}$
1.658×10^5	$(8.99 \pm 0.08) \times 10^{-2}$	$(6.15 \pm 0.06) \times 10^{-2}$
2.131×10^5	$(9.28 \pm 0.04) \times 10^{-2}$	$(5.92 \pm 0.12) \times 10^{-2}$
2.739×10^5	$(7.67 \pm 0.02) \times 10^{-2}$	$(4.84 \pm 0.08) \times 10^{-2}$
3.52×10^5	$(5.21 \pm 0.14) \times 10^{-2}$	$(3.06 \pm 0.07) \times 10^{-2}$
4.523×10^5	$(3.25 \pm 0.16) \times 10^{-2}$	$(1.70 \pm 0.15) \times 10^{-2}$

Table S 1: The final SDWFS power spectrum values $l^2 C_l / 2\pi$ for both the 3.6 μm and 4.5 μm bands. The quoted error is the 1 σ uncertainty of the final power spectrum.

A matrix correction method exists³⁷ to model the effects of the mask on the power spectrum by using a matrix $M_{ll'}$ whose inverse removes the effects of the mask from the measurement by matrix multiplication. If \tilde{C}_l is the masked sky power spectrum and C_l be the true power spectrum, the relation between the true and masked sky spectrum is

$$\tilde{C}_l = M_{ll'} C_{l'} \quad , \quad (8)$$

where Einstein summation notation is being used. Since this relationship is matrix multiplication, the masking effects can be removed from the masked power spectrum by simply using a matrix multiplication $M_{ll'}^{-1} \tilde{C}_l$ to recover the true power spectrum C_l . In the limit of no l -mode coupling, $M_{ll'} = f_{\text{sky}}$ where f_{sky} is the fraction of the masked map that is non-zero.

Calculating the mode coupling matrix $M_{ll'}$ analytically³⁷ is computationally expensive for large maps. For this reason, we developed a new way to generate the mode-coupling matrix as follows:

1. For each ℓ in the power spectrum create many realizations of maps consisting of a pure tone where $C_m = 1$ if $\ell = m$ and $C_m = 0$ otherwise (an example case is shown in Fig. S9).
2. For each of these trial maps, mask the maps and calculate an observed power spectrum $\tilde{C}_m(\ell)$.
3. The mode coupling matrix $M_{\ell m} = \langle \tilde{C}_m(\ell) \rangle$ is the average of the masked power spectra found for the random realizations of model ℓ . The inverse of the mode coupling matrix gives the sky power spectrum corrected for the masking effect, $C_l = M_{lm}^{-1} \tilde{C}_m$.

To see how well this works, consider Fig. S9. The black line shows the exact power spectrum from which we drew 100 simulated images. The red points show the observed power spectra of the masked sky. The blue points show those same 100 power spectra after correcting with the mode coupling matrix described above. This mode-coupling transformation does an excellent job recovering the input power spectra of an unmasked sky. As the lower panel of Fig. S9 shows using the simplified model based only on the masked sky fraction f_{sky} is not a good approximation.

To estimate the effects of cosmic variance on the power spectrum one must make multiple Gaussian simulations with the exact power spectrum measured in the data. Without applying a mask, these simulations will have a cosmic variance:

$$\delta C_l^{\text{CV}} = \sqrt{\frac{2}{(2l+1)\delta l f_{\text{sky}}}} C_l \quad (9)$$

where δC_l^{CV} is the cosmic variance for multipole l , δl is the width of that l bin, f_{sky} is the fraction of the total sky covered by the unmasked region, and l in the denominator is the mid-point of the

l bin. It should be clear that masks should increase cosmic variance because they further reduce the coverage of the unmasked sky. The mode-coupling matrix does not restore errors from cosmic variance and therefore, masking and correcting with $(M_{ll'})^{-1}$ will combine errors from the mode-coupling matrix as well as the reduced coverage from the mask and thus have a greater variance than cosmic variance alone.

6 The Map-making Transfer Function

The last correction that must be accounted for is to correct for the effects of the map-making procedure in producing the final mosaic. The mosaicing procedure is often combines many images and between dealing with overlap regions as well adding more tiles to a mosaic, the addition or subtraction of total power must be quantified and corrected. The best way to uncover the effects of the mosaicing procedure on the power spectrum is to take a map with a known power spectrum, re-build the map using your mosaicing procedure and compare the output and input power spectra. More specifically to build the map-making transfer function we followed the following procedure:

1. We created a large map similar in size, pixel scale and astrometry to our SDWFS data mosaic, but assuming a shape for the power spectrum (we started with pure white noise for which $C_l = \text{constant}$).
2. We break the map into the tiles similar in size, pixel scale and astrometry to our original data tiles. We added instrumental noise to the tiles consistent with the noise of the different epochs.
3. We ran these simulated signal plus noise tiles through the same self-calibration mosaicing procedure described in Section 1 to produce a new map identical to the original map modulo the mosaicing effects.
4. The map-making transfer function is then $T_l = C_l^{\text{orig}}/C_l^{\text{mosiaced}}$, where C_l^{orig} is the known power spectrum of the original simulation and C_l^{mosiaced} is the power of the final map.
5. We repeated Steps 1 to 4 above for different initial power spectra to test if the transfer function remains the same or is different. We found that the transfer function is independent of the assumption for the input power spectrum shape or the amplitude.

For our analysis we used this process with the self-calibration algorithm for the mosaic transfer function. Simulated maps of pure white noise broken into tiles and remosaiced using the self-calibration algorithm to determine the transfer functions. An example transfer function for SDWFS is given in Fig. S10. This was obtained by simulating 10^3 independent maps and using the mean and the standard deviation of $(T_l)_i$, where i denotes each simulation, to determine the best-determined transfer function and its error.

Given the transfer function T_l , beam correction b_l , the mode-coupling matrix $M_{ll'}$ the final power spectrum is estimated as

$$C_l = M_{ll'}^{-1} T_l' \tilde{C}_{l'} / b_l^2 \quad (10)$$

where $\tilde{C}_{l'}$ is the raw power spectrum after masking out the foreground sources and C_l is the final corrected power spectrum. C_l is the power spectrum that we present in the main paper and compared to previous results.

7 Final Power Spectrum Results

To compute the power spectrum for the infrared background at $3.6 \mu\text{m}$ we used all four epochs of the SDWFS data as described above. In order to minimize contamination from instrumental noise, zodiacal light and other systematics we used the cross-correlation $1/2(E_1 + E_2) \times 1/2(E_3 + E_4)$ and the two additional permutations by switching the epochs, where $E_1..E_4$ correspond to the four epochs. Masks were generated to remove the foreground and applied as described above before the cross-correlations were taken. We used the same cross-correlation procedure to obtain the $4.5 \mu\text{m}$ power spectrum. After the raw spectra are obtained from the mosaics, they are corrected for the beam, mode-coupling, mosaicing (or map-making) effects as described above using Equation 10.

Fig. S11 shows the results from the *Spitzer* SDWFS Boötes field (the power spectra values are listed in Table 1). Results from a recent analysis¹² are also given for reference. These spectra are the final spectra after all corrections have been applied. We note the strong agreement between our measurements and the previously published ones. The difference at small angular scales, high ℓ , is due to differences in the depth of the mask. It is captured by a difference of the shot-noise levels in the point source detection level between SDWFS and deeper SEDS data¹².

Fig. S12 shows the angular cross-power spectrum of near-IR anisotropies measured with SDWFS at 3.6 and $4.5 \mu\text{m}$. The left panel shows the cross power spectrum ($C_l^{3.6-4.5}$) between the two channels, while the right panel shows the correlation coefficient calculated as

$$r = C_l^{3.6-4.5} / \sqrt{C_l^{3.6} C_l^{4.5}}, \quad (11)$$

where $C_l^{3.6}$ and $C_l^{4.5}$ are the auto power spectra at 3.6 and $4.5 \mu\text{m}$, respectively (Fig. S11). The correlation coefficient is consistent with unity. The errors are the 1σ overall uncertainty in the correlation coefficients found by propagating errors on the cross power spectrum and auto power spectra through equation 11.

8 Theoretical Interpretation of Near-IR Anisotropies as Spatial Fluctuations of Integrated Intrahalo Light

Our intrahalo light (IHL) model presented in the *Letter* is described in this Section. In Fig. 1 of the main *Letter*, we also show results from two descriptions related to the near-IR background

anisotropies. One involves the faint galaxies that fall below the magnitude cut-off of the masks that are applied to measure fluctuations. The contribution from faint galaxies, primarily dwarf has been studied in detail with latest information on the faint-end of the galaxy luminosity functions⁷ and we use their results in Fig. 1. A second model involves the $z > 6$ galaxy contribution. The shaded region for $z > 6$ galaxies in Fig. 1 combines the analytical models¹⁹ with results from numerical simulations²⁰. The predictions are normalized to the measured luminosity functions of galaxies at $z > 6$ and uses a reionization history that is consistent with the WMAP 7-year optical depth to electron scattering¹⁹.

For the interpretation presented in the *Letter*, we model the IHL intensity angular power spectrum using the halo model. The IHL model differs from galaxy clustering models in that we assign a profile to the diffuse stars. The standard galaxy clustering models assume a central galaxy at the halo center and satellites that are distributed randomly in the halo with a profile that is tracing the dark matter distribution. We now add a diffuse extended component in addition to the central and satellite galaxies. The halo number density⁴³ as a function of redshift and mass $dn(M, z)/dM$ is

$$\frac{dn}{d \ln M} = \frac{\rho_m}{M} f(\nu) \frac{d\nu}{d \ln M}, \quad (12)$$

with

$$\nu f(\nu) = A \sqrt{\frac{2}{\pi}} a \nu^2 [1 + (a \nu^2)^{-p}] \exp[-a \nu^2 / 2]. \quad (13)$$

Given a galaxy luminosity-halo mass relation, a certain fraction $f_{ICL}(M)$ of this luminosity will be in the form of IHL. The IHL luminosity-mass relation is then:

$$L_{IHL,\lambda}(M, z) = f_{IHL}(M) L(M, z = 0) (1 + z)^\alpha f_\lambda(\lambda / (1 + z)), \quad (14)$$

where α is the power-law index that accounts for a possible redshift evolution and $f_\lambda(\lambda / (1 + z))$ is the spectral energy distribution of the IHL (see also discussion below). We model the fraction of total luminosity in form of IHL as a power-law in halo mass,

$$f_{IHL}(M) = A_f \left(\frac{M}{10^{12} M_\odot} \right)^\beta. \quad (15)$$

The total luminosity as a function of halo-mass $L(M, z = 0)$ at $z = 0$ is taken to be the best-fit relation from⁴⁶ at $2.2 \mu\text{m}$

$$L(M, z = 0) = 5.64 \cdot 10^{12} h_{70}^{-2} \left(\frac{M}{2.7 \cdot 10^{14} h_{70}^{-1} M_\odot} \right)^{0.72} L_\odot. \quad (16)$$

This is measured for galaxy groups and clusters. At smaller mass scales one no longer has the issue of multiple galaxies in a halo and the total luminosity is simply that of the central galaxy⁴⁷. We

extend it to lower masses using the same power-law slope since analyses of the total luminosity-halo mass relation using galaxy-galaxy lensing find the slope continues down to mass scales below $10^{11} M_{\odot}$ ^{48,49}. Given that this total luminosity-halo mass relation is measured at $2.2 \mu\text{m}$, we scale this to other wavelengths with the SED f_{λ} , but with the normalization that $f_{\lambda} = 1$ at $2.2 \mu\text{m}$ at $z = 0$. We consider the SED of IHL to be consistent with that of old elliptical galaxies comprised of old, red stars⁴⁴. In the main *Letter*, in Fig. 3, we also consider alternatives for the SED using a variety of galaxy SED templates.

Under these assumptions the angular power spectrum of the IHL flux fluctuations can be written as the sum of a 1-halo term, that originates from small-scale fluctuations within individual halos

$$C_{\ell}^{1h} = \frac{1}{(4\pi)^2} \int dV \frac{1}{(1+z)^2 \chi^4(z)} \int_{M_{min}}^{M_{max}} dM \frac{dn(M, z)}{dM} u_{\text{IHL}}^2(k|M) L_{\text{IHL}, \lambda}^2(M, z), \quad (17)$$

and a 2-halo term, related to the large scales dark matter fluctuations, and hence to the linear dark matter power spectrum $P_M(k, z)$ as

$$C_{\ell}^{2h} = \frac{1}{(4\pi)^2} \int dV \frac{1}{(1+z)^2 \chi^4(z)} \left[\int_{M_{min}}^{M_{max}} dM \frac{dn(M, z)}{dM} u_{\text{IHL}}(k|M) b_h(M, z) L_{\text{IHL}, \lambda}(M, z) \right]^2 \times P_M(k = \ell/\chi(z), z), \quad (18)$$

where $u_{\text{IHL}}(k, z|M)$ is the Fourier transform of the IHL profile in a dark matter halo of mass M at redshift z , $b_h(M)$ is the linear bias, $\chi(z)$ is the comoving radial distance, and dV is the comoving volume element $dV = \chi(z)^2 d\chi/dz$. The redshift integration is performed up to a maximum redshift $z_{\text{max}} = 5$. We found that integrating to a higher redshift did not change our results. The values of M_{min} and M_{max} in Eqs. 17 and 18 determine the relative amplitude of the 1-halo and 2-halo terms and we let them vary freely. The power spectrum also contains a shot-noise contribution from unresolved fluctuations, so that the total power spectrum is

$$C_{\ell} = C_{\ell}^{1h} + C_{\ell}^{2h} + C_{\ell}^{\text{SN}}. \quad (19)$$

We also take C_{ℓ}^{SN} to be a free parameter that is varied during our model fitting.

Since the IHL profile for small mass halos has yet to be determined precisely, we consider two model descriptions under the assumption that IHL (i) traces the Navarro-Frenk-White (NFW) profile of dark matter halos⁵⁰ and (ii) falls as r^{-2} with an exponential cut-off⁵¹ such that $\rho_{\text{IHL}} \propto 1/r^2 \exp(-r/2R_{\text{vir}})$. There is limited information on the light profile from the stacking analysis of SDSS galaxies⁵². However, we are unable to use those measurements for the current study as we do not have information on how the profile changes with the halo mass. Moreover given the limited information both in terms of the angular scale of fluctuations and the large uncertainties we find that we are not able to statistically distinguish one IHL profile over another.

In Fig. 1 of the main *Letter*, the best-fit anisotropy power spectrum makes use of the description involving the NFW profile with

$$\rho(r) = \frac{\rho_s}{(cr/r_{\text{vir}})(1 + cr/r_{\text{vir}})^2}, \quad (20)$$

where r_{vir} is the virial radius and c the halo concentration parameter. We define the concentration using the result from numerical simulations³⁹ that find

$$c(M, z) = \frac{9}{1+z} \left(\frac{M}{M_*} \right)^{-0.13}, \quad (21)$$

where M_* is the mass scale at which the critical density contrast δ_c required for spherical collapse is equal to the square root of the variance in the initial density field $\sigma(M_*) = \delta_c$. While we make use of this particular fitting function³⁹, an alternative fitting function⁴⁰ led to the same results. Thus, our best-fit parameter values are independent of the assumption on the halo mass-concentration relation.

To analyze the data we conducted a Monte Carlo-Markov Chain (MCMC) analysis using a modified version of the publicly available package cosmoMC⁴⁵ with convergence diagnostic based on the Gelman-Rubin statistic⁴¹. We fit a total of six free parameters: the minimum and maximum masses (M_{min} , M_{max}), the power-law index of the redshift dependence in the luminosity-mass relation α , the amplitude and the power-law index with halo mass of the IHL fraction A_f and β , respectively, and the shot noise contribution C_ℓ^{SN} . We fix the cosmological parameters to the best-fit for the Λ CDM concordance model from WMAP 7-year analysis⁴².

The best-fit parameters for the fit to the data at $3.6 \mu\text{m}$ from SDWFS are shown in Table 6. The minimum and maximum halo masses of the halo mass range contributing to measured near-IR anisotropies is $10^{9.03 \pm 0.05} M_\odot$ and $10^{11.91 \pm 0.05} M_\odot$, respectively. Our model-fitting suggests a small dependence of the IHL fraction on halo mass with a power-law slope of $\beta = 0.09 \pm 0.01$. We found values consistent with the 1σ uncertainties when using the alternate IHL profile described above and fitting the model to the $4.5 \mu\text{m}$ power spectrum measurements. Our results for $f_{\text{IHL}}(M)$ are summarized in Fig. 2 of the main *Letter*. There we also compare our determination to an analytical prediction of the IHL fraction relative to the total luminosity, in the literature¹⁴. These analytical models exist only down to a halo mass scale of about $5 \times 10^{10} M_\odot$ and $f_{\text{IHL}} > 5 \times 10^{-4}$. In addition to the power-law behavior it was found also found in previous analytical work¹³ that the IHL fraction is constant at a value of about 0.005 when $M < 5 \times 10^{11} M_\odot$ in some scenarios to generate IHL. This flattening behavior could be related to our observation that the IHL fraction is not strongly halo mass dependent over the mass ranges that we are probing with near-IR background anisotropy power spectrum. More detailed studies are necessary to properly understand how our results can be used to understand the merger rate and generation of IHL in low mass halos at redshifts of 1 to 4.

In Fig. S13 we summarize the redshift dependence of the IHL power spectrum by calculating dC_l/dz as a function of redshift. The contributions peak at a redshift of 3, but has a broad distri-

bution ranging from $1 < z < 4$. The measured shot-noise level of 120 ± 10 nJy nW m⁻² sr⁻¹ is about a factor of 2 higher than the shot-noise in the deeper SEDS data¹² with a value of ~ 57 nJy nW m⁻² sr⁻¹.

In Fig. 3 of the main *Letter*, we summarize the SED of IHL. Here, we make use of a variety of stellar templates from B to K-type stars for this purpose. The prediction converges at the longer wavelengths due to existing measurements but we find large deviations at 1 μ m and shorter wavelengths. A measurement of the background anisotropy at optical wavelengths is clearly desirable and could be used to both identify the stars that are primarily contributing to IHL at $z \sim 1$ to 4.

9 References

31. Eisenhardt, P. R. et al. The Infrared Array Camera (IRAC) Shallow Survey, *Astrophys. J. Suppl.* 154, 48-53 (2004).
32. Makovoz, D. & Khan, I. 2005, *Astronomical Data Analysis Software and Systems*, *Astronomical Society of Pacific Conference Series* 132, *Astronomical Data Analysis Software and Systems VI*, edited by P. L. Shopbell, M. C. Britton, & R. Ebert (San Francisco: ASP).
33. Fixsen, D. J., Moseley, S. H. & Arendt, R. G. Calibrating Array Detectors, *Astrophys. J. Suppl.* 128, 651 (2000).
34. Quijada, M. A., Marx, C. T., Arendt, R. G. & Moseley, S. H. 2004, Angle-of-incidence effects in the spectral performance of the infrared array camera of the Spitzer Space Telescope, *Optical, Infrared, and Millimeter Space Telescopes*. Edited by Mather, John C. *Proceedings of the SPIE*, 5487, 244-252 (2004).
35. Bertin, E. & Arnouts, S. SExtractor: Software for source extraction. *Astron. and Astroph. Suppl.* 317, 393 (1996).
36. Arendt, R. G., Kashlinsky, A., Moseley, S. H. & Mather, J. Cosmic Infrared Background Fluctuations in Deep Spitzer IRAC Images: Data Processing and Analysis, *Astrophys. J. Suppl.* 186, 10-47 (2010).
37. Hivon, E. et al. MASTER of the Cosmic Microwave Background Anisotropy Power Spectrum: A Fast Method for Statistical Analysis of Large and Complex Cosmic Microwave Background Data Sets, *Astrophys. J.* 567, 2-17 (2002).
38. Sullivan, I. et al. Clustering of the IR Background Light with Spitzer: Contribution from Resolved Sources, *Astrophys. J.* 657, 37-50 (2007).
39. Bullock J. S. et al. Profiles of dark haloes: evolution, scatter and environment, *Mon. Not. R. Astron. Soc.*, 321, 559-575 (2001).

40. Duffy, A. R., Schaye, J., Kay, S. T. & Della Vecchia, C. 2008, Dark matter halo concentrations in the Wilkinson Microwave Anisotropy Probe year 5 cosmology, *Mon. Not. of the Roy. Astron. Soc.*, 390, L64-L68 (2008).
41. Gelman A. & Rubin. D. B. Inference from Iterative Simulation Using Multiple Sequences, *Statist. Sci.* 7, 457-472 (1992).
42. Komatsu E. et al. Seven-year Wilkinson Microwave Anisotropy Probe (WMAP) Observations: Cosmological Interpretation, *Astrophys. J. Suppl.* 192, 18 (2011).
43. Sheth R. K. & Tormen G. Large-scale bias and the peak background split, *Mon. Not. R. Astron. Soc.*, 308, 119-126 (1999).
44. Krick J. E. & Bernstein R. A. Diffuse Optical Light in Galaxy Clusters. II. Correlations with Cluster Properties, *Astrophys. J.* 134, 466-493 (2007).
45. Lewis A. & Bridle S. Cosmological parameters from CMB and other data: A Monte Carlo approach, *Phys. Rev. D* 66, 103511 (2002).
46. Lin Y. -T. , Mohr J. J. & Stanford S. A. K-Band Properties of Galaxy Clusters and Groups: Luminosity Function, Radial Distribution, and Halo Occupation Number, *Astrophys. J.* 610, 745-761 (2004).
47. Vale, A. & Ostriker, J. P. Linking halo mass to galaxy luminosity, *Mon. Not. of the Roy. Astron. Soc.*, 353, 189-200 (2004).
48. Cooray, A. & Milosavljević, M. Dissipationless Merging and the Assembly of Central Galaxies, *Astrophys. J.* 627, L85-L88 (2005).
49. Yang, X., Mo, H. J., van den Bosch, F. C. Constraining galaxy formation and cosmology with the conditional luminosity function of galaxies, *Mon. Not. of the Roy. Astron. Soc.*, 339, 1057-1080 (2003).
50. Navarro J. F., Frenk C. S. & White S. D. M. A Universal Density Profile from Hierarchical Clustering, *Astrophys. J.*, 490, 493 (1997)
51. Masaki, S. & Yoshida, N. Distribution of Dust around Galaxies: An Analytic Model, [arXiv.org:1203.6414](https://arxiv.org/abs/1203.6414) (2012).
52. Tal, T. & Dokkum, P. The faint stellar halos of massive red galaxies from stacks of more than 42000 SDSS LRG images, *Astrophys. J.* 731, 89 (2011).

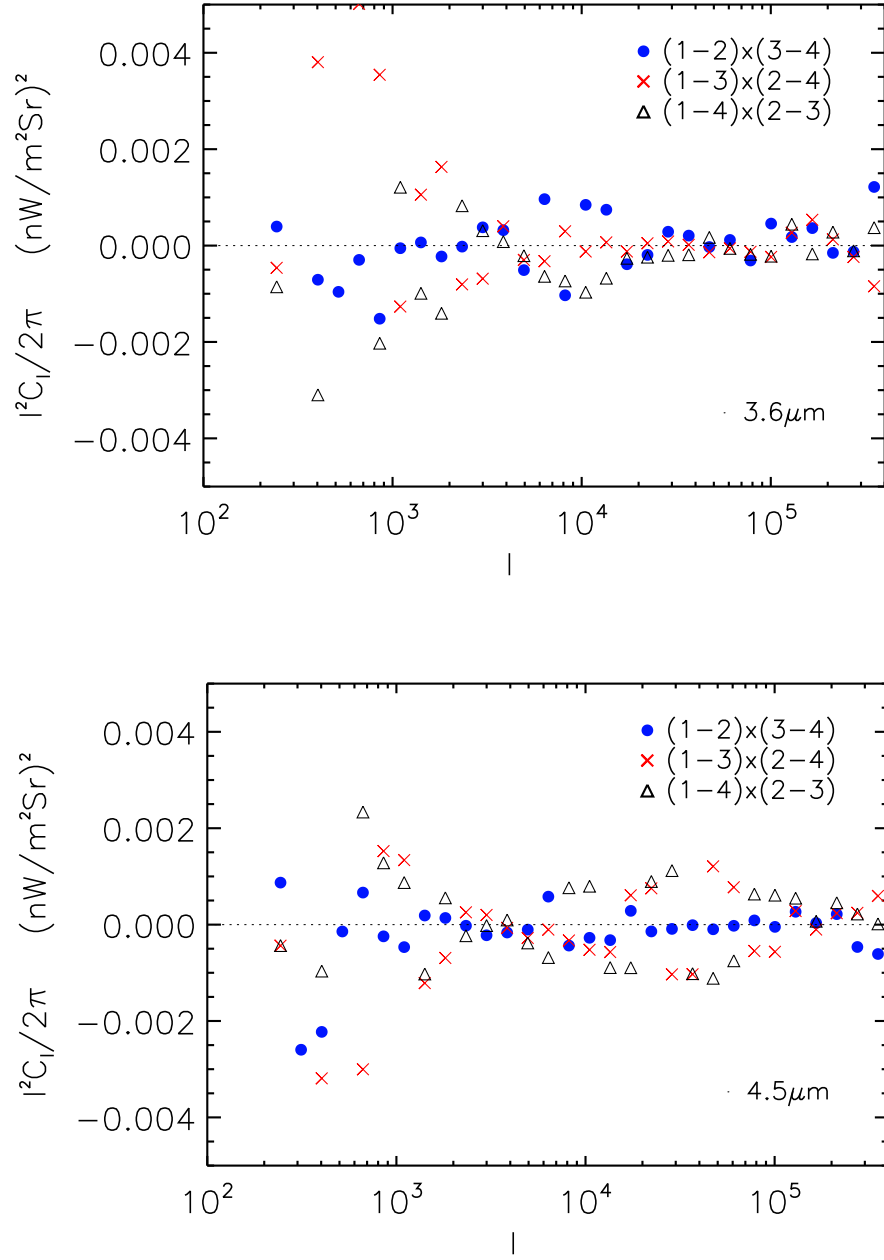


Figure S 4: **The cross power spectra of the difference of multi-epoch maps.** The cross-correlation power spectra of the difference of multi-epoch maps between epochs 1 to 4 with $3.6\mu\text{m}$ (top) and $4.5\mu\text{m}$ (bottom) shown separately. The cross-correlations are consistent with zero and the variance between the different cross-correlations provide one part of the final error budget associated with the power spectrum measurement.

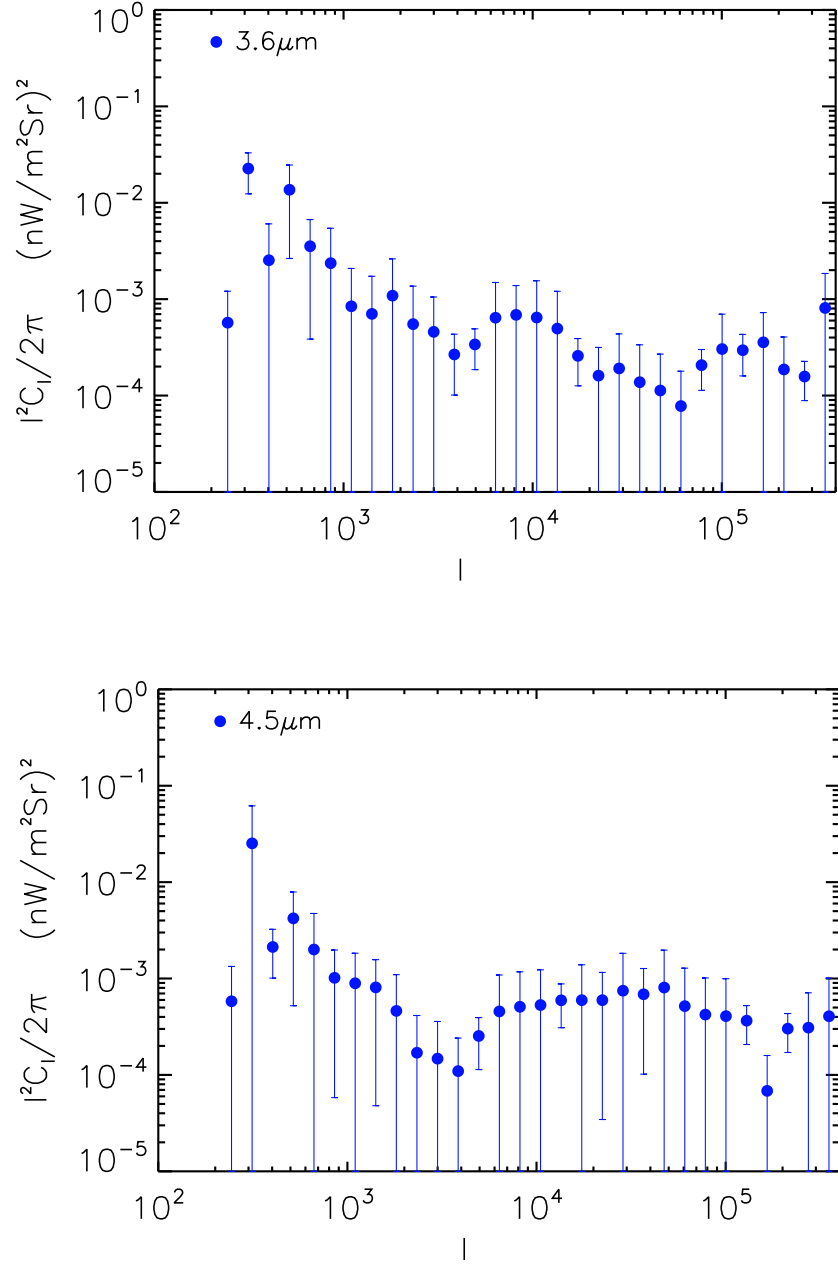


Figure S 5: **The noise floor to detect near-IR background anisotropies.** The mean and the variance (1σ) of the different-epoch difference maps cross-correlations. We show the absolute value of the mean and the error on the mean from the variance of the three independent cross-correlations.

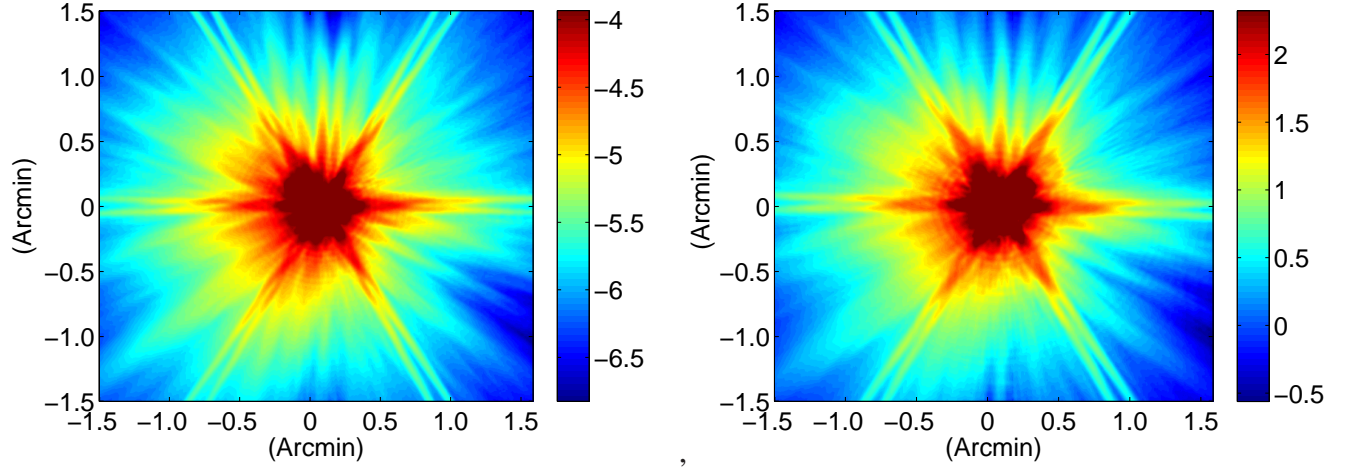


Figure S 6: **The IRAC PSF.** The $3.6\ \mu\text{m}$ (left) and $4.5\ \mu\text{m}$ (right) IRAC PSFs on a logarithmic intensity scale.

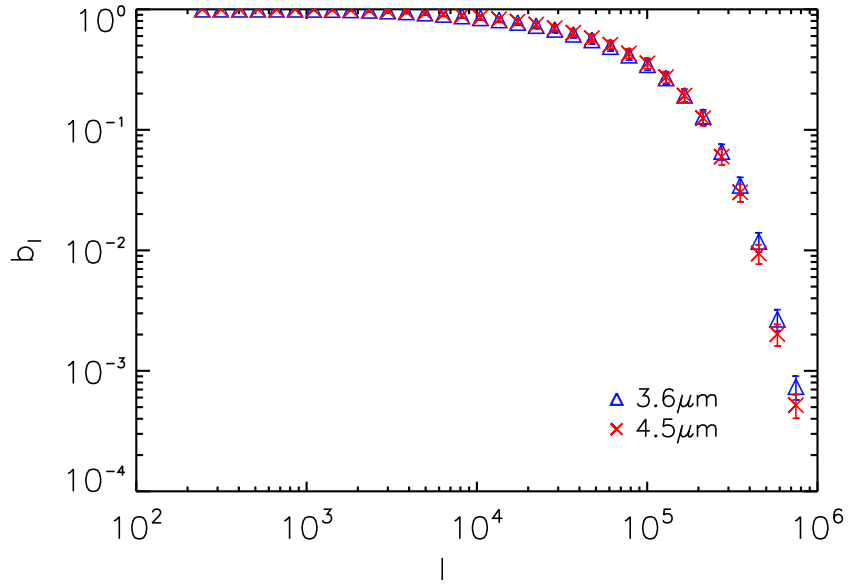


Figure S 7: **The IRAC beam function.** The beam transfer functions for the SDWFS Boötes field in the multipole space ℓ . We show the functions at $3.6\ \mu\text{m}$ and $4.5\ \mu\text{m}$ with triangles and crosses, respectively. The plotted error bars are the $1\ \sigma$ uncertainties.

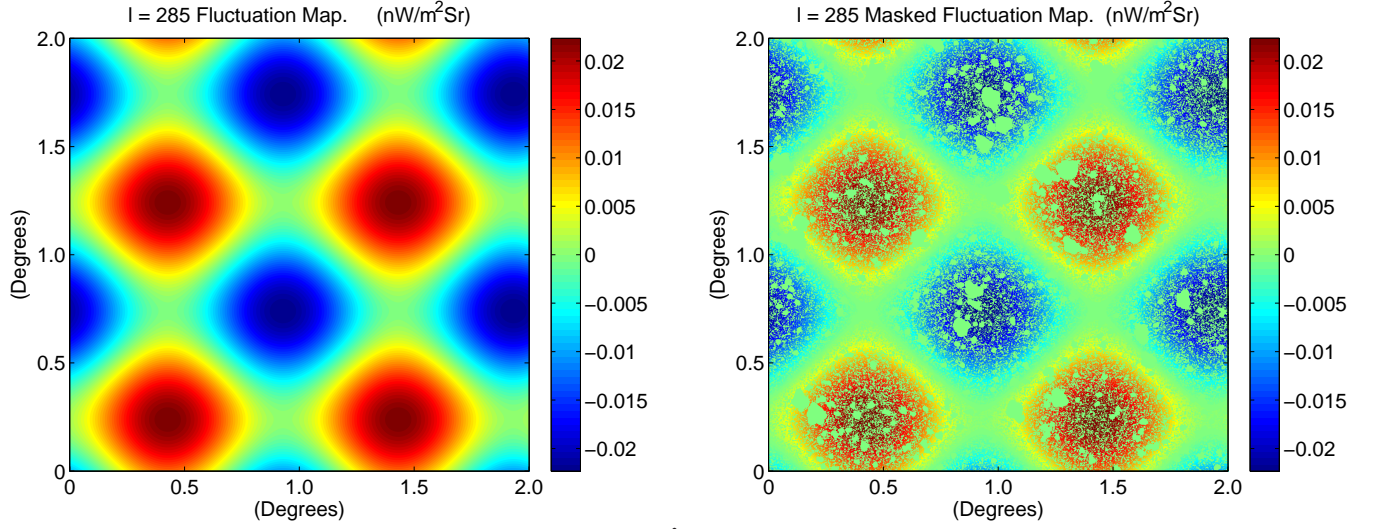


Figure S 8: **The masking effects in a map.** The left shows a map of a $l = 285$ fluctuation. On the right is the same map masked by one of the SDWFS masks. Note how what was only a large scale fluctuation gets broken up into smaller modes by the mask, contaminating the true power.

A_f	0.0015 ± 0.0002
$\log(M_{\min}/M_{\odot})$	9.03 ± 0.05
$\log(M_{\max}/M_{\odot})$	11.91 ± 0.05
β	0.094 ± 0.005
α	1.23 ± 0.09
$C_{\ell}^{\text{SN}} (\text{nW}^2 \text{ m}^{-4} \text{ sr}^{-1})$	$(9.8 \pm 0.5) \times 10^{-11}$

Table S 2: The best-fit parameter values of the IHL anisotropy power spectrum model to the $3.6 \mu\text{m}$ data using MCMC model fits. The quoted error bars are the 1σ uncertainties for each of the parameter likelihoods marginalizing over other parameters.

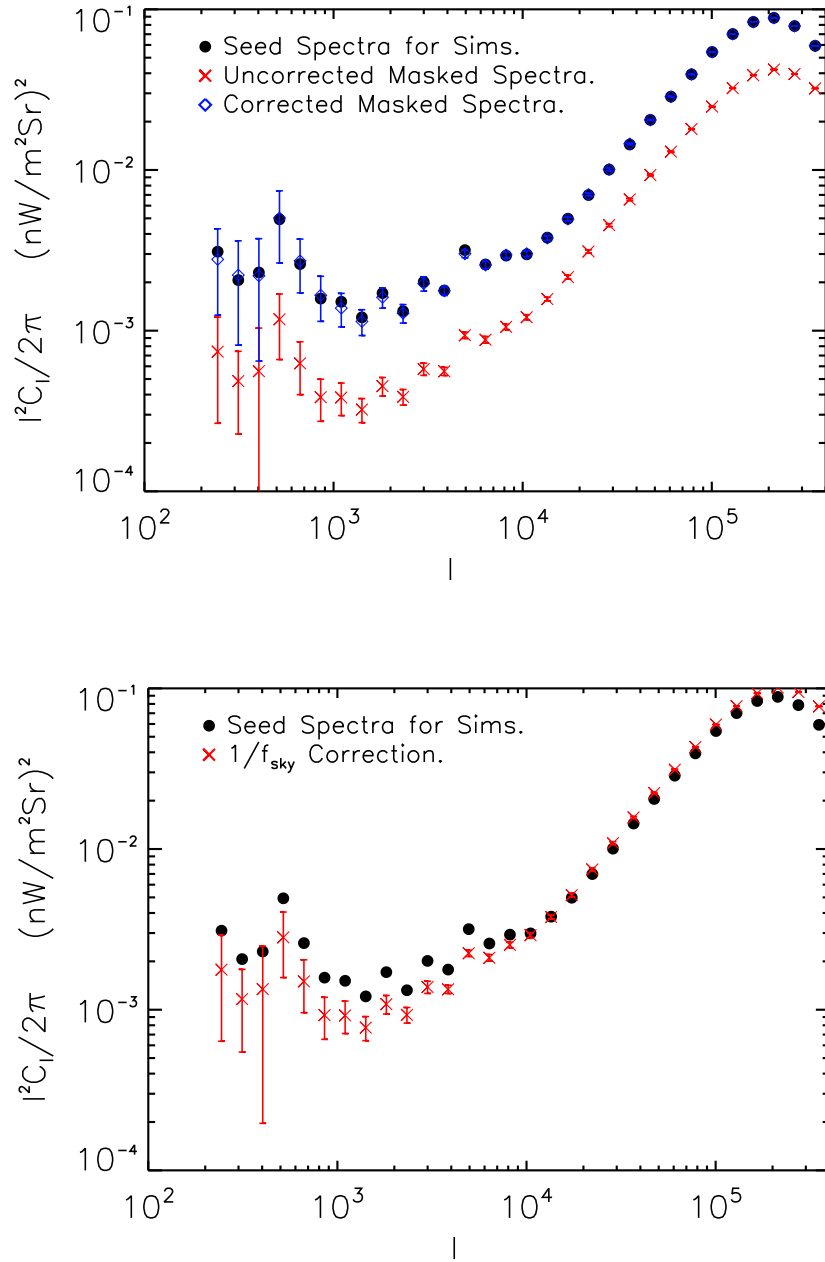


Figure S 9: **Masking effects on the power spectrum.** The top panel shows how well we can recover the true spectrum of a masked sky using the mode coupling matrix. The black points show the seeded spectra we used to create 100 simulations. The red shows what happens to the spectra after masking using the $3.6 \mu\text{m}$ mask. The blue points show what happens after correcting with the mode-coupling matrix. The bottom panel shows the result if corrected with only the masked sky fraction given by f_{sky} . The mask breaks many large modes into smaller modes, so that after the f_{sky} correction the large-scale modes are under-represented and the small-scale modes are over-represented. This illustrates the need to use the full coupling matrix to correct for the mask. The plotted error bars are the 1σ uncertainties.

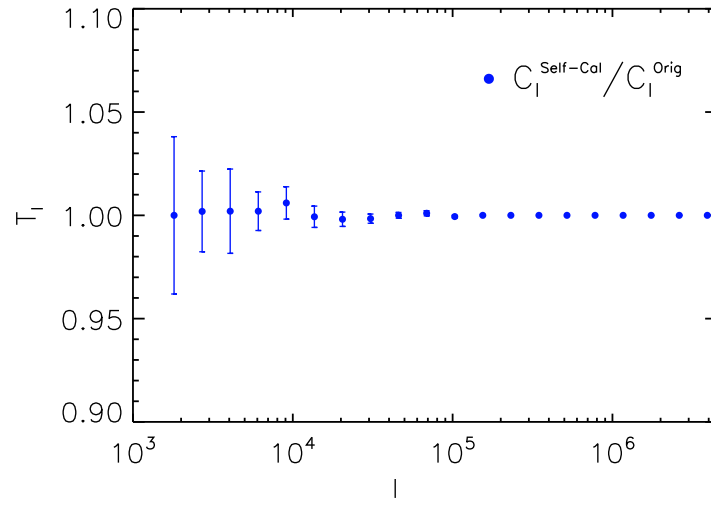


Figure S 10: **The map-making transfer function.** *Spitzer*-IRAC mosaic transfer function based on the self-calibration algorithm used to make data maps for this study. We show the transfer function at $3.6 \mu\text{m}$. The $4.5 \mu\text{m}$ transfer function is similar to the result at $3.6 \mu\text{m}$. The plotted error bars are the 1σ uncertainties.

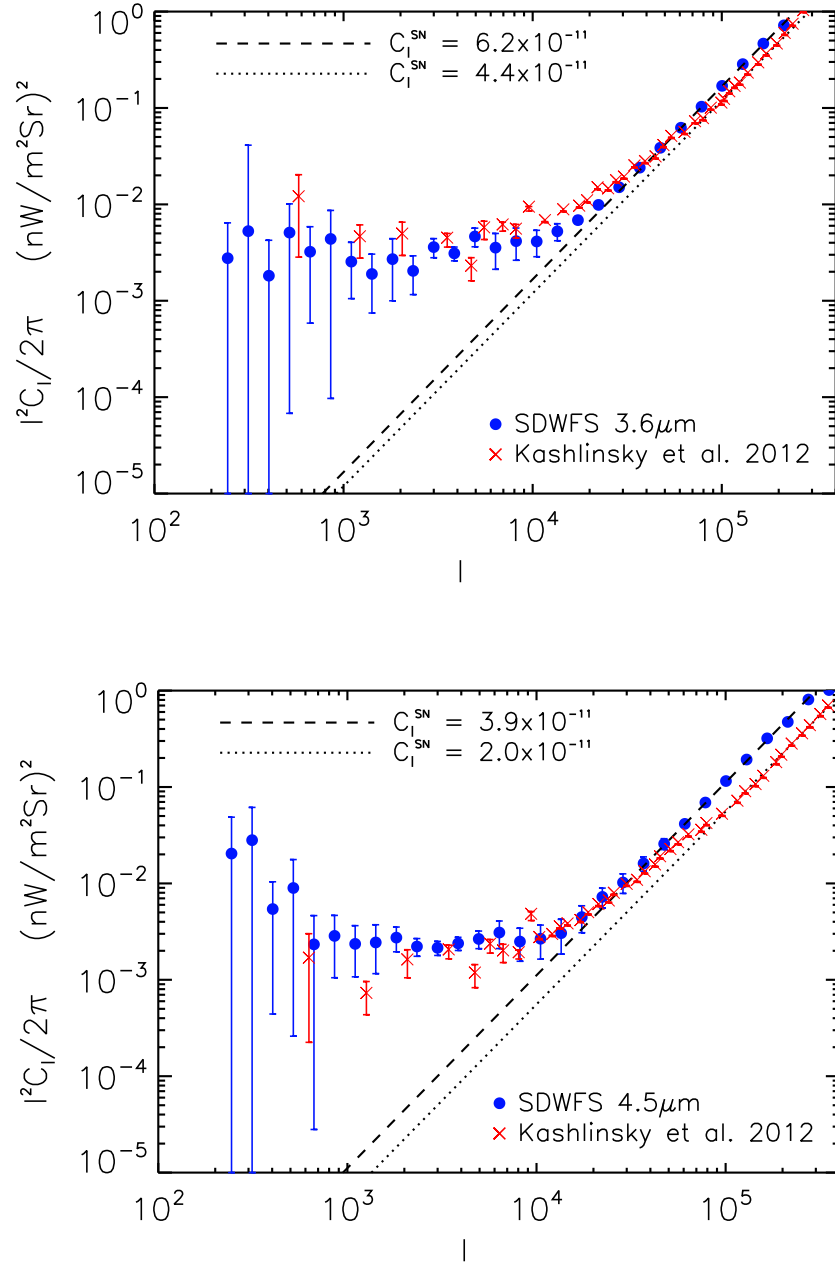


Figure S 11: **The angular power spectrum of near-IR anisotropies.** The angular power spectrum of near-IR anisotropies measured with SDWFS at 3.6 and 4.5 μm . The 1σ error bars include all uncertainties we have discussed in the Supplement and the measurements are beam corrected. We also compare our measurements to existing results¹² where we find a general agreement on clustering. The large- ℓ difference between the two datasets reflect the depth of the point source identification and removal in the mask.

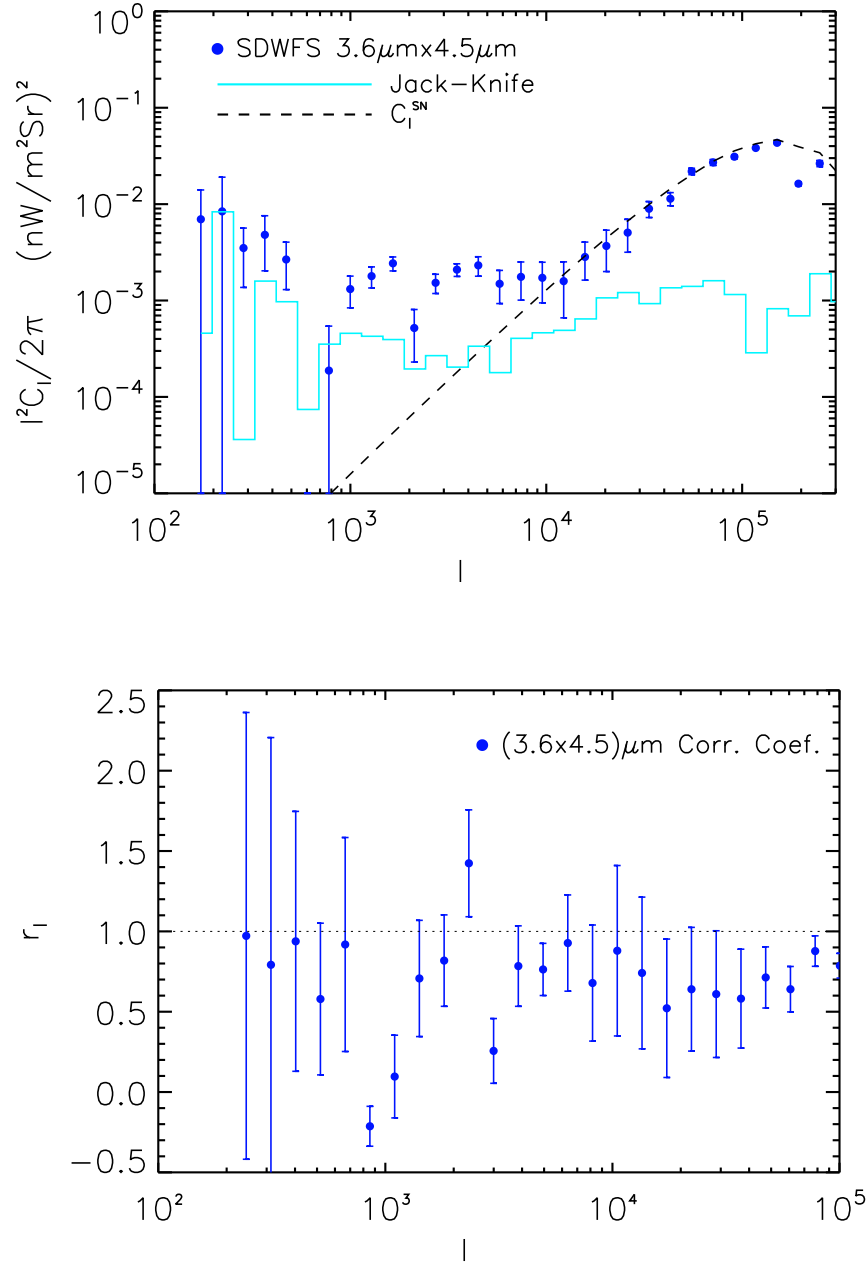


Figure S 12: **The angular cross-power spectrum of near-IR anisotropies.** The angular cross-power spectrum of near-IR anisotropies measured with SDWFS at 3.6 and 4.5 μm . The 1σ error bars include all uncertainties we have discussed in the Supplement and the measurements are beam corrected. The upper panel shows the cross power spectrum ($C_l^{3.6-4.5}$), while the lower panel shows the correlation coefficient calculated as $r = C_l^{3.6-4.5}/\sqrt{C_l^{3.6}C_l^{4.5}}$, where $C_l^{3.6}$ and $C_l^{4.5}$ are the auto power spectra at 3.6 and 4.5 μm , respectively (Fig. S11)

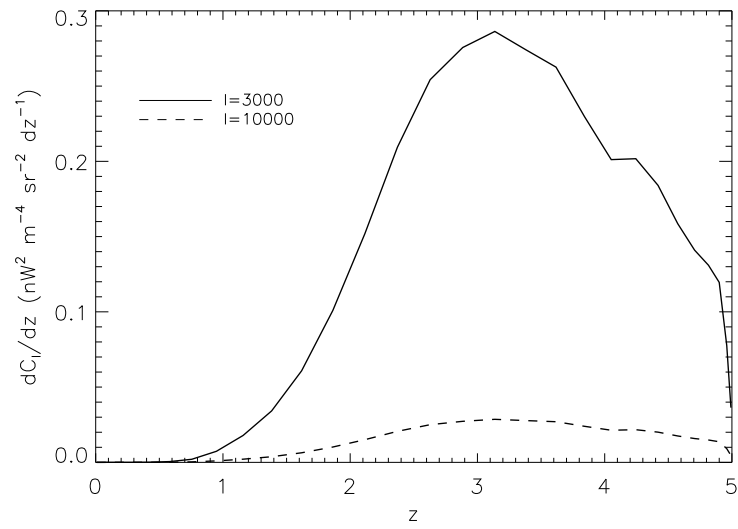


Figure S 13: **The redshift dependence of the IHL anisotropy power spectrum.** dC_l/dz as a function of redshift for $\ell = 3 \times 10^3$ and 10^4 . The majority of near-IR anisotropies originate from $1 < z < 4$.